Failure of heterogeneous materials: 3D meso-scale FE models with embedded discontinuities — Source link [↗]

Nathan Benkemoun, Martin Hautefeuille, Martin Hautefeuille, Jean-Baptiste Colliat ...+1 more authors

Institutions: École normale supérieure de Cachan, Braunschweig University of Technology

Related papers:

- Anisotropic constitutive model of plasticity capable of accounting for details of meso-structure of two-phase composite material

- An analysis of strong discontinuities induced by strain-softening in rate-independent inelastic solids

- Mesoscale models for concrete: homogenisation and damage behaviour

- Embedded discontinuity finite element method for modeling of localized failure in heterogeneous materials with structured mesh: an alternative to extended finite element method

- A finite element method for localized failure analysis

Modeling heterogeneous materials failure: 3D meso-scale models with embedded discontinuities

Nathan Benkemoun, Martin Hautefeuille, Jean-Baptiste Colliat, Adnan Ibrahimbegovic

Modeling heterogeneous materials failure: 3D meso-scale models with embedded discontinuities

N. Benkemoun, M. Hautefeuille, J.-B. Colliat and A. Ibrahimbegović

LMT-Cachan (ENS-Cachan/CNRS/UPMC/PRES UniverSud Paris)
61 avenue du Président Wilson, 94235 Cachan Cedex, France

Abstract

We present a meso-scale heterogeneous model adapted to quasi-brittle materials such as concrete and based on spatial truss representation. In order to explicitly incorporate heterogeneities without using adapted meshes, some bar elements need to be split into two parts. To that respect both weak and strong discontinuities are embedded into those elements using the Incompatible Mode Method and a dedicated local solution procedure based on the operator split is described. Several macroscopic loading paths are then considered, showing quite complex macroscopic responses though the mesoscopic failure criterion is voluntary chosen as simple as possible.

Key words: heterogeneous materials, failure models, embedded discontinuity, incompatible modes method

1 Introduction

Modeling inelastic behavior of heterogeneous materials is strongly related to the observation scale. From a macro scale point of view, the usual engineering approach considers most of these materials as homogeneous, tacitly introducing the Representative Volume Element concept [1] and leading to the widely used phenomenological models, such as plasticity and damage. Those models are based on macroscopic quantities (macroscopic stresses and strains)and macroscopic laws derived in a thermodynamical framework [2]. Considering

---

cement based materials such as concrete, there is an extensive literature (see [3] for a review) dealing with its mechanical behavior modeling according to different loading paths, for static or dynamical case as well as several multi-physics couplings, such as heat or water mass transfers. However, most of the physical phenomena and the failure mechanisms which can be observed for such materials are taking place at finer scales. Ideally, we would like to resolve one of the major issue dealing with concrete, hoping to establish a (numerical) link between the initial constituants properties and the resulting mechanical properties at macroscale. Such a bridge would require a very precise and accurate description of the hardened material microstructure, exhibiting several phases and the ability to use such description as, for example, a finite element model.

At the so-called meso scale, heterogeneous materials such as concrete might be modeled with two or three different phases at least; the macroscopic mechanical response of such materials will obviously depends on each phase properties as well as their spatial distribution and shapes. Being able to compute such macroscopic global response by taking account for the mesoscopic phases is a major issue related to the high number of degrees-of-freedom arising, the numerical localization due to softening and the interfaces behavior. In this paper, the approach we focus on is able to cope with both of those challenges dealing with 3D problems. This approach relies on spatial truss models, geometrically built using Delaunay triangulation. In order to model heterogeneities such as inclusions, strain field (weak) discontinuities are introduced inside the bar elements which are "cut" by an interface (see Fig. 1). Hence each element might be split in two parts, each having different elastic properties. Thus the nodes spatial positions are not constrained by the physical interfaces and, consequently, the meshing process (i.e. the Delaunay triangulation) does not depend on the inclusions positions and shapes. Considering a two-phases material where inclusions are melt into a matrix, three sets of elements are needed: those entirely lying inside the matrix (first set, with the same elastic modulus and no strain discontinuity) or inside the inclusions (second set) and those which are split by a physical interface and for which the strain discontinuity is activated (third set). Such modeling strategy allows to represent any heterogeneous material in the elastic regime, with any number of phases and with a very fast and efficient meshing process. Based on this geometrical representation and in order to model the non-linear softening response shown by brittle and quasi-brittle materials, displacement (strong) discontinuities are also introduced inside the bar element. These discontinuities represents micro-cracks that may occur in any of different phases (inclusions or matrix for a two-phases material) and also allows to capture the interface failure (debonding) which might appear between any phase. Moreover, the key point pertains to strong discontinuities capability to model softening behavior without any mesh dependancy (see [4], [5]), which is a major issue dealing with failure of quasi-brittle materials.
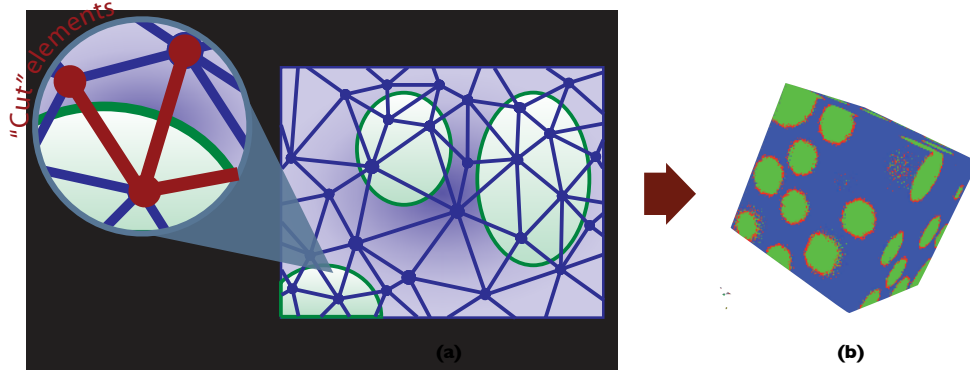
Fig. 1. Two-phases material with split elements (a) and 3D random meso-structure (b) : matrix-blue, green-inclusion and red-interface

Among different possibilities to enhance the kinematics and thus to introduce both weak and strong discontinuities within the Finite Element model ([5], [6] [7], [8], [9], [10]) we choose the Incompatible Modes Method ([11], [12]). The latter provides the main advantage in no requirement for any modification of the Finite Element code global structure and the total number of unknowns as well.

The outline of the paper is as follows: In Section 2 we introduce the mesoscale model, with the truss element, as well as the numerical implementation details according to the Incompatible Modes Method. Then, in Part 3, we turn to the macroscopic scale by describing the numerical responses to different macroscopic loading paths.

2 Meso-scale model

As stated in the introduction, the meso-scale model presented in this paper for heterogeneous materials relies on truss elements with enhanced kinematics. These enhancements concern both the strain field (in order to represent an elastic modulus jump [13], [14]) and the displacement field (in order to model cracks through displacements jumps [4], [15], [16], [17]). This Section describes these two kinds of discontinuities and shows how the Incompatible Modes Method ([11], [12]) might be used to accomodate both of these jumps.

3

2.1 Kinematics enhancements

2.1.1 Weak discontinuity: heterogeneous materials

Dealing with heterogeneous materials and not adapted meshes lead to the possibility for an element to be split into two parts, each with different elastic properties (see Fig. 1). From a computational point of view, two subdomains need to be defined inside the element by positioning the interface between these two parts (its spatial position is parametrized using the adimensional parameter θ). This idea is the key point for the first kinematics enhancement, described by the function $\boldsymbol{G}_1$. Fig. 2 shows that $\boldsymbol{G}_1$ presents a finite strain jump at the interface (in red) between the two subdomains of a typical truss element with different elastic properties.
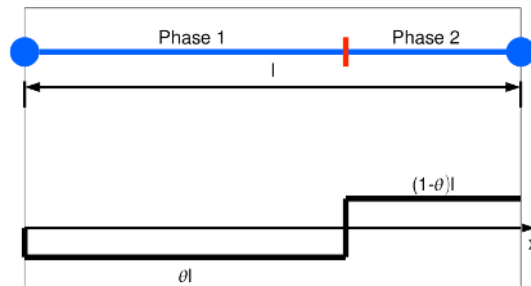

Fig. 2. Split truss element with weak discontinuity and $\boldsymbol{G}_1$ function

The strain-displacement function $\boldsymbol{G}_1$ may be written as:

$$\boldsymbol{G}_1 = \begin{cases} -\frac{1}{\theta\ell} \ , \ \ x \in [0, \theta\ell] \\[2ex] \frac{1}{\ell(1-\theta)} \ , \ \ x \in [\theta\ell, \ell] \end{cases}$$

It is worth to mention that the same enhancement can also be employed for several other physical properties of heterogeneous materials, such as condtuctive heat transfer where the elements can be split in two parts with different values of thermal conductivity coefficient.

2.1.2 Strong discontinuity: quasi-brittle materials cracking

Modeling the cracking process for brittle and quasi-brittle materials is a major issue. Actually, the softening behavior due to cracks opening leads to mesh dependancy and many authors ([4], [5]) have shown that representing cracks by using strong discontinuities allows to get rid of such pathology. Moreover it allows to introduce the fracture energy G_f (which represents the energy needed to fully open a $1\,m^2$ fracture) among the model parameters set. Fig. 3 shows the second kinematics enhancement, represented by the function denoted as

$\boldsymbol{G}_2$. This function exhibits a jump at the interface position, between the two subdomains, and can thus represents the debonding phenomenon.
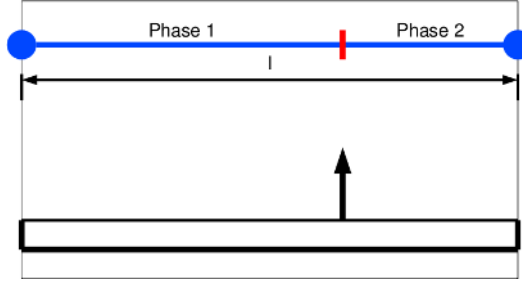

Fig. 3. Split truss element with strong discontinuity and $\boldsymbol{G}_2$ function

The function $\boldsymbol{G}_2$ can be written:

$$\boldsymbol{G}_2 = -\frac{1}{\ell} + \delta_\Gamma$$

where δ_Γ is the Dirac function placed at the interface. In the following, $\boldsymbol{G}_2$ will be split into a regular part $\bar{\boldsymbol{G}}_2 = -\frac{1}{\ell}$ and a non-regular part $\bar{\bar{\boldsymbol{G}}}_2 = \delta_\Gamma$.

Finally, the key idea here is to use enhanced elements with strong discontinuities in every element, and not only placed at the interface. This leads to the capability to represent cracking in every phase of the materials, and not only debonding.

2.2 Theorical framework: Incompatible Mode Method

The Hu-Washizu variational formulation ([18], [19]) applied to the enhanced strain method [11] provides a suitable theorical framework in order to enhance elements kinematics: the strain field is written as the sum of the displacement symmetric gradient $\nabla^s u$ and the enhanced strains $\tilde{\epsilon}_1$ and $\tilde{\epsilon}_2$,

$$\epsilon = \nabla^s u + \tilde{\epsilon}_1 + \tilde{\epsilon}_2$$

Using the classical truss element shape functions [20] as well as the two functions $\boldsymbol{G}_1$ and $\boldsymbol{G}_2$ introduced previously, the variational formulation can be written within the framework of a finite element problem and leads to the following set of non-linear equations,

$$\begin{cases} \mathbf{A}_{e=1}^{n_{elm}} \left[\mathbf{f}_e^{int}(\boldsymbol{d}_e, \alpha_{1,e}, \alpha_{2,e}) - \mathbf{f}_e^{ext} \right] = \mathbf{0} & \text{global equilibrium equation} \\ \mathbf{h}_{1,e}(\boldsymbol{d}_e, \alpha_{1,e}, \alpha_{2,e}) = \mathbf{0} \quad \forall e \in [1, n_{elm}] & \text{local equilibrium equation} \\ \mathbf{h}_{2,e}(\boldsymbol{d}_e, \alpha_{1,e}, \alpha_{2,e}) = \mathbf{0} \quad \forall e \in [1, n_{elm}] & \text{local equilibrium equation} \end{cases} \quad (1)$$

where $\mathbf{A}$ denotes the standard assembly operator. The explicit form of element arrays can be written,

$$\mathbf{f}_e^{int} = \int_{\Omega_e} \boldsymbol{B}^T \boldsymbol{\sigma} (\boldsymbol{B}\boldsymbol{d}_e + \boldsymbol{G}_1 \alpha_{1,e} + \bar{\boldsymbol{G}}_2 \alpha_{2,e}) \, \mathrm{d}V$$

$$\mathbf{h}_{1,e} = \int_{\Omega_e} \tilde{\boldsymbol{G}}_1^T \boldsymbol{\sigma} (\boldsymbol{B}\boldsymbol{d}_e + \boldsymbol{G}_1 \alpha_{1,e} + \bar{\boldsymbol{G}}_2 \alpha_{2,e}) dV$$

$$\mathbf{h}_{2,e} = \int_{\Omega_e} \tilde{\boldsymbol{G}}_2^T \boldsymbol{\sigma} (\boldsymbol{B}\boldsymbol{d}_e + \boldsymbol{G}_1 \alpha_{1,e} + \bar{\boldsymbol{G}}_2 \alpha_{2,e}) dV$$

where $\tilde{\boldsymbol{G}}_{(1,2)}^T$ are modified version functions of $\boldsymbol{G}_{(1,2)}$ in order to fulfil the patch test ([12]), and write as follows:

$$\tilde{\boldsymbol{G}}_{(1,2)}^T = \boldsymbol{G}_{(1,2)} - \frac{1}{\Omega^e} \int_{\Omega^e} \boldsymbol{G}_{(1,2)} dV$$

In (1), $\alpha_{1,e}$ and $\alpha_{2,e}$ are the interpolation parameters corresponding to both weak and strong discontinuities. These two parameters are defined independently for each element so that they are local quantities only (from a FE point of view). It is worth noting that only the second of equations (1), which concerns the weak discontinuity enhancement, is a linear equation. Moreover, we note that the strong discontinuity is introduced only upon reaching a fracture criterion, so that the third equation in system (1) is not always present.

2.2.1 Failure criterion

Dealing with brittle and quasi-brittle materials, the yield function Φ used to activate the strong discontinuity is written as:

$$\Phi = t_\Gamma - (\sigma_f - q)$$

where t_Γ is the traction vector at the discontinuity and σ_f the limit stress. The softening is introduced through the variable $q = \mathrm{k}(\alpha_2)$ by considering the exponential form,

$$\mathrm{k}(\alpha_2) = \sigma_f \left(1 - \exp \left(-\frac{\alpha_2}{G_f} \right) \right)$$

we introduced the fracture energy G_f as the area under t_Γ α_2 curve (recall that α_2 is the crack opening). The key point here is that such failure criterion is triggered only for fracture in tension.

2.2.2 Linearization

Incorporating the yield function equation as suggested by [21] , the non-linear system (1) can be extended to:

$$
\begin{cases}
\mathbf{A}_{e=1}^{n_{elm}} \left[\mathbf{f}_e^{int}(\boldsymbol{d}_e, \alpha_{1,e}, \alpha_{2,e}) - \mathbf{f}_e^{ext} \right] = \mathbf{0} & \text{global equilibrium equation} \\
\mathbf{h}_{1,e}(\boldsymbol{d}_e, \alpha_{1,e}, \alpha_{2,e}) = \mathbf{0} \quad \forall e \in [1, n_{elm}] & \text{local equilibrium equation} \\
\mathbf{h}_{2,e}(\boldsymbol{d}_e, \alpha_{1,e}, \alpha_{2,e}) = \mathbf{0} \quad \forall e \in [1, n_{elm}] & \text{local equilibrium equation} \\
\Phi(t_\Gamma, \alpha_{2,e}) = 0 \quad \forall e \in [1, n_{elm}] & \text{local failure criterion}
\end{cases}
\tag{2}
$$

By further replacing the expressions for $\tilde{\boldsymbol{G}}_1$, $\tilde{\boldsymbol{G}}_2$ and $\boldsymbol{B}$ into (2), we can obtain,

$$
\begin{cases}
\mathbf{A}_{e=1}^{n_{elm}} \left[\mathbf{f}_e^{int}(\boldsymbol{d}_e, \alpha_{1,e}, \alpha_{2,e}) - \mathbf{f}_e^{ext} \right] = \mathbf{0} & \\
-\sigma_1(\boldsymbol{d}_e, \alpha_{1,e}, \alpha_{2,e}) + \sigma_2(\boldsymbol{d}_e, \alpha_{1,e}, \alpha_{2,e}) = 0 & \forall e \in [1, n_{elm}] \\
\theta \sigma_1(\boldsymbol{d}_e, \alpha_{1,e}, \alpha_{2,e}) + (1 - \theta)\sigma_2(\boldsymbol{d}_e, \alpha_{1,e}, \alpha_{2,e}) - t_\Gamma = 0 & \forall e \in [1, n_{elm}] \\
\Phi(t_\Gamma, \alpha_{2,e}) = 0 & \forall e \in [1, n_{elm}]
\end{cases}
\tag{3}
$$

where σ_1 and σ_2 are the stresses in each subdomain of the element, and t_Γ the traction vector at the discontinuity. We recall that the scalar value θ parametrizes the discontinuity spatial position.

The key point here is to note that the third of equations (3) provides a direct and explicit form for t_Γ in terms of:

$$
t_\Gamma = \theta \sigma_1(\boldsymbol{d}_e, \alpha_{1,e}, \alpha_{2,e}) + (1 - \theta)\sigma_2(\boldsymbol{d}_e, \alpha_{1,e}, \alpha_{2,e})
$$

Therefore, the final set of equation can be reduced to,

$$
\begin{cases}
\mathbf{A}_{e=1}^{n_{elm}} \left[\mathbf{f}_e^{int}(\boldsymbol{d}_e, \alpha_{1,e}, \alpha_{2,e}) - \mathbf{f}_e^{ext} \right] = \mathbf{0} & \\
-\sigma_1(\boldsymbol{d}_e, \alpha_{1,e}, \alpha_{2,e}) + \sigma_2(\boldsymbol{d}_e, \alpha_{1,e}, \alpha_{2,e}) = 0 & \forall e \in [1, n_{elm}] \\
\Phi(t_\Gamma, \alpha_{2,e}) = 0 & \forall e \in [1, n_{elm}]
\end{cases}
\tag{4}
$$

to be solved for $\boldsymbol{d}_e$, $\alpha_{1,e}$ and $\alpha_{2,e}$. Here again only the second equation in (4) is linear. Linearization of (4) at the given values of $(\boldsymbol{d}_e, \alpha_{1,e}, \alpha_{2,e})$ yields to the following linear system:

$$
\begin{pmatrix}
\mathbf{a} & \mathbf{b} & \mathbf{c} \\
\mathbf{b^T} & d & e \\
-\mathbf{c^T} & -e & f(\alpha_2)
\end{pmatrix}_{n+1}^{(k)}
\begin{pmatrix}
\Delta \boldsymbol{d} \\
\Delta \alpha_1 \\
\Delta \alpha_2
\end{pmatrix}_{n+1}^{(k+1)}
=
\begin{pmatrix}
-\mathbf{A}_{e=1}^{n_{elm}} \left[\mathbf{f}_e^{int}(\boldsymbol{d}_e, \alpha_{1,e}, \alpha_{2,e}) - \mathbf{f}_e^{ext} \right] \\
-\mathbf{h}_{1,e} \\
-\Phi
\end{pmatrix}_{n+1}^{(k)}
$$

where

$$\mathbf{a} = \boldsymbol{B}^T E_1 \boldsymbol{B} \theta \ell^e + \boldsymbol{B}^T E_2 \boldsymbol{B} (1-\theta)\ell^e \quad \mathbf{b} = \boldsymbol{B}^T[-E_1 + E_2]$$

$$\mathbf{c} = -\boldsymbol{B}^T[\theta E_1 + (1-\theta)E_2] \qquad d = \frac{E_1}{\theta \ell^e} + \frac{E_2}{(1-\theta)\ell^e}$$

$$e = \frac{1}{\ell^e}(E_1 - E_2) \qquad f(\alpha_2) = [-\frac{\theta E_1}{\ell^e} - \frac{(1-\theta)E_2}{\ell^e}] - k'(\alpha_2)$$

The complete solution procedure for computing $\Delta \boldsymbol{d}^{(k+1)}$, $\Delta \alpha_1^{(k+1)}$ and $\Delta \alpha_2^{(k+1)}$ is presented in more details in the next section.

2.3 Solution procedure: operator split mehod

The solution procedure operates on two levels: the global level, corresponding to the first equation of (5) and the local level. In the spirit of the operator split method, $\Delta \alpha_1^{(k+1)}$ and $\Delta \alpha_2^{(k+1)}$ are computed first from the local phase at fixed value for $\boldsymbol{d}_{n+1}$. Once this first stage has been completed, the static condensation is performed of these two variables $\Delta \alpha_1^{(k+1)}$ and $\Delta \alpha_2^{(k+1)}$, leading to a standard global equilibrium system of linear equations with a modified stiffness matrix.

2.3.1 Local level of operator-split computation

The algorithm dealing with the local level proceeds as follows:

Recall that the weak discontinuity equation is linear. Thus there is no need to iterate for $\Delta \alpha_1^{(j+1)}$ which is computed directly (see step 4 in Alg. (1)).

2.3.2 Double static condensation

Once the local phase of computation has converged, both residuals $\mathbf{h}_1$ and Φ are equal to zero. Thus the system (5) can be rewritten as,

$$\begin{pmatrix} \mathbf{a} & \mathbf{b} & \mathbf{c} \\ \mathbf{b^T} & d & e \\ -\mathbf{c^T} & -e & f(\alpha_2) \end{pmatrix}_{n+1}^{(k)} \begin{pmatrix} \Delta \boldsymbol{d} \\ \Delta \alpha_1 \\ \Delta \alpha_2 \end{pmatrix}_{n+1}^{(k+1)} = \begin{pmatrix} -\mathbf{A}_{e=1}^{n_{elm}} \left[\mathbf{f}_e^{int}(\boldsymbol{d}_e, \alpha_{1,e}, \alpha_{2,e}) - \mathbf{f}_e^{ext} \right] \\ 0 \\ 0 \end{pmatrix}_{n+1}^{(k)}$$

where $\Delta \alpha_1$ and $\Delta \alpha_2$ are both known. The second step consists in performing the static condensation ([22]) for $\Delta \alpha_1^{(k+1)}$ and $\Delta \alpha_2^{(k+1)}$, leading to a linear

---

Algorithm 1 Operator split at the element level

1: **while** $[\text{abs}(\dfrac{\Phi^{(j)}.\Delta\alpha_2^{(j+1)}}{\Phi^{(0)}.\Delta\alpha_2^{(1)}}) > \text{tol and } j < j_{max}]$ **do**

2:   linear weak discontinuity

3:   `residual computation:` $\text{h}_1{}^{(j)} = -\sigma_1^{(j)} + \sigma_2^{(j)}$

4:   `increment computation:` $\Delta\alpha_1^{(j+1)} = -\dfrac{\text{h}_1{}^{(j)}}{\frac{E_1}{\theta\ell^e} + \frac{E_2}{(1-\theta)\ell^e}}$

5:   `update:` $\alpha_1^{(j+1)} = \alpha_1^{(j)} + \Delta\alpha_1^{(j+1)}$

6:   `update intermediate values:` $\tilde\sigma_1^{(j+1)}$, $\tilde\sigma_2^{(j+1)}$, $\tilde\Phi^{(j+1)}$

7:   **if** $(j == 0 \text{ and } \tilde\Phi^{(j+1)} > 0)$ **then** (iloc == 1) **else** (iloc == 0)

8:   **if** (iloc == 0) **then**

9:     break while loop

10:     $\sigma_1^{(j+1)} = \tilde\sigma_1^{(j+1)}, \sigma_2^{(j+1)} = \tilde\sigma_2^{(j+1)}$

11:   **end if**

12:   **if** (iloc == 1) **then**

13:     non $-$ linear strong discontinuity

14:     `increment computation:` $\Delta\alpha_2^{(j+1)} = -\dfrac{\tilde\Phi^{(j+1)}}{[-\frac{\theta E_1}{\ell^e} - \frac{(1-\theta)E_2}{\ell^e}] - k'(\alpha_2^{(j)})}$

15:     `update:` $\alpha_2^{(j+1)} = \alpha_2^{(j)} + \Delta\alpha_2^{(j+1)}$

16:     `update:` $\sigma_1^{(j+1)}$, $\sigma_2^{(j+1)}$, $\Phi^{(j+1)}$

17:   **end if**

18:   $j + +$

19: **end while**

---

system based on the matrix $\hat{\mathbf{K}}$. Solving this global system of linear equations provides the displacement increment $\Delta\boldsymbol{d}_{n+1}^{(k+1)}$:

$$\hat{\mathbf{K}}^{(k)}\Delta\boldsymbol{d}^{(k+1)} = -\mathbf{A}_{e=1}^{n_{elm}}\left[\mathbf{f}_e^{int}(\boldsymbol{d}_e, \alpha_{1,e}, \alpha_{2,e}) - \mathbf{f}_e^{ext}\right]^{(k)}$$

where the condensed stiffness matrix is written as:

$$\hat{\mathbf{K}} = \mathbf{a} - \left[\frac{1}{d.f(\alpha_2)+e^2}\right]\begin{bmatrix} \mathbf{b} & \mathbf{c} \end{bmatrix}\begin{bmatrix} f(\alpha_2) & -e \\ e & d \end{bmatrix}\begin{bmatrix} \mathbf{b}^{\mathbf{T}} \\ -\mathbf{c}^{\mathbf{T}} \end{bmatrix}$$

It is worth noting that the total number of unknows for the global system remains constant, and is not influenced by the kinematics enhancements. All those improvements will only influence the element level. This is one of the major advantages of the Incompatible Modes Method.

3 Macroscopic model response

In this section, we present the macroscopic responses for several loading paths. All of these computations have been done using the *Feap* CTL component *coFeap* ([23], [24], [25]). We first provide some details dealing with the mesh generation and then turn to the macroscopic behaviors in both tensile, compression and shear.

3.1 Geometry description and mesh generation

As presented in the second Part, the approach we present in this paper relies on spatial truss models at meso-scale. Such truss can be generated by computing the 3D Delaunay triangulation of a Poisson point process over the spatial domain of interest and according to a prescribed points density. Each edge of the obtained tethraedral elements is converted to a bar element whose cross section is computed by mean of the corresponding Voronoi tesselation. Such task is carried out by using *Qhull* ([26]) which is a general dimension code for computing convex hulls, Delaunay triangulations and Voronoi diagrams. Finally, spherical inclusions are generated by mean of a Gibbs point process and according to both prescribed density and radius. These inclusions are incorporated within the spatial truss by computing their intersections with each bar element, denoted in the previous part by θ. The key point is that this last step is completely independent from the truss generation itself, which is a much more time consuming process. Hence such mesh generation methodology shall be very efficient for any probabilistic numerical analysis considering a stochastic geometry description.

One typical example of a mesh that can be obtained is shown in Fig. 4. Here we consider two phases materials only thus leading to three kinds of bar elements. Obviously, such methodology can be extented to more heterogeneous materials, with a high number of different phases, although the total number of elements families would rapidly increase.

3.2 Tension test 3D macroscopic response

As a first case of study, we present here the macroscopic responses obtained for a concrete-like two phases material along simple tension loading paths, along the three axes and hydrostatic as well.
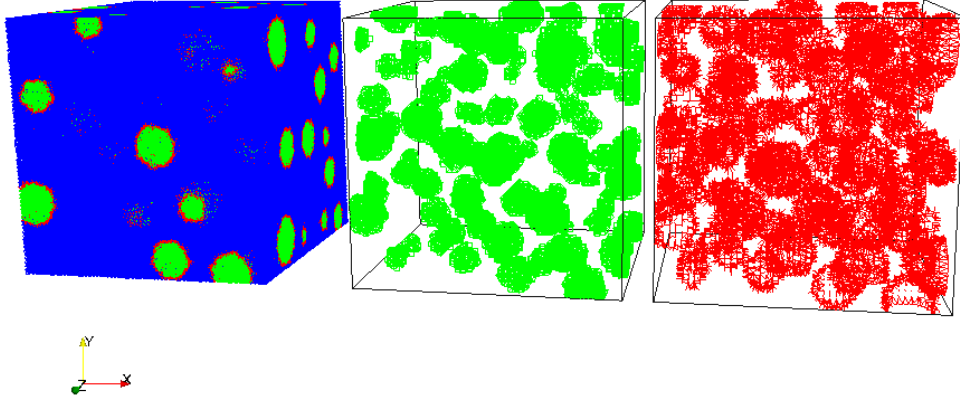
Fig. 4. Spatial truss for a typical two phases material: matrix blue, inclusions green, red interface

3.2.1 1D tension test and mesh objectivity

Dealing with 1D tension we consider here a $0.001\,m^3$ cube. Tab.1 sums up both physical and geometrical parameters for each phase. One can note that inclusions are stiffer than the cementeous matrix and that they remain in the elastic regime. This computation is made under displacement control according to the first spatial axis.

cementeous matrix	inclusions	interfaces
$E = 10$ GPa	70 GPa	-
$\sigma_f = 2$ MPa	-	2 MPa
$G_f = 9\,\mathrm{J/m^2}$	-	$9\,\mathrm{J/m^2}$
volume	inclusions vol. fraction (%)	dof
$10^{-3}\,\mathrm{m^3}$	34	~ 300000

Table 1
1D tension test geometry and materials parameters

Fig. 5a shows the macroscopic load (sum of all nodal reactions in the X-direction) versus imposed displacement curve. The macroscopic Young modulus is equal to 29900 MPa and the macroscopic limit stress which triggers softening is equal to 1.8 MPa. On Fig. 5b, we show the micro-cracked bar elements (for whose the strong discontinuity has been activated). It is worth noting that Fig. 5b shows some kind of a macro-crack that lies in the direction

11

roughly perpendicular to the imposed displacement one. This crack is pictured from two differents points of view: First in the displacement field along the X-direction where two blocks appear (sudden change of the color code) as separated by the macro-crack; secondly by the mean of the broken elements, where we observe only all the elements split by the activated displacement discontinuity which then merged together providing a clear representation of the macro-crack. Moreover we can note that the macro-crack is tortuous, around the inclusions that remain elastic. Finally, Fig. 5b shows that only one macro-crack is sufficient to drive the macroscopic response into the softening regime.
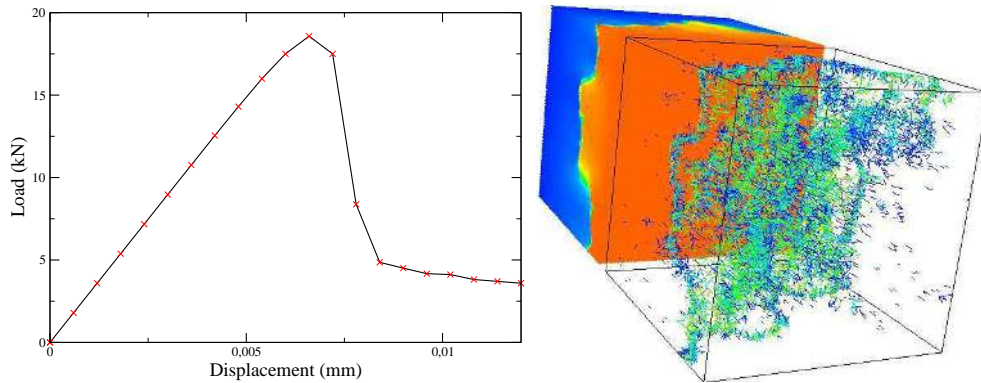

Fig. 5. 1D traction a. macroscopic load vs displacement curve, b. contours of displacement field in X-direction and micro-cracks pattern at the end of the computation

Based on this 1D traction test, the next point we present here deals with the mesh objectivity that is one of the major issue for softening behaviors. Fig. 6 shows the macroscopic forces versus imposed displacement responses obtained from three different meshes with increasing number of nodes. We can note that all the essential macroscopic properties, such as the macroscopic stiffness, the macroscopic peak resistance and the amount of dissipated energy, remain practically mesh-invariant as soon as the sufficient mesh refinement is achieved (around 300000 dof).
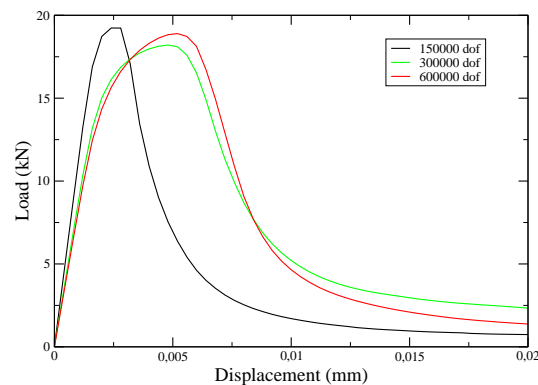

Fig. 6. Macroscopic load vs displacement response showing mesh objectivity of the computed response

Finally, this simple 1D tension test has been repeated along the two other axes in order to assess for the mesh generation process isotropy. Fig. 7a shows the macroscopic load (sum of all nodal reactions in the X-direction (black), in the Y-direction (red) and in the Z-direction (green)) versus imposed displacement curves. We note that, whatever the imposed displacement direction is, the macroscopic modulus (31000 MPa) and the macroscopic peak stress remain unchanged. Fig. 7b, here again, pictures all micro-cracks at the end of the computation, providing a clear representation of the apparent macro-crack for each loading path. Here again it is worth noting that a single macro-crack appears, roughly orthogonal to the imposed displacement direction.

cementeous matrix	inclusions	interfaces
$E = 10$ GPa	70 GPa	-
$\sigma_f = 2$ MPa	-	2 MPa
$G_f = 9\,\mathrm{J/m^2}$	-	$9\,\mathrm{J/m^2}$
volume	inclusions vol. fraction (%)	dof
$10^{-3}\,\mathrm{m^3}$	34	~ 600000

Table 2
1D tension test along X, Y and Z direction: geometry and materials parameters
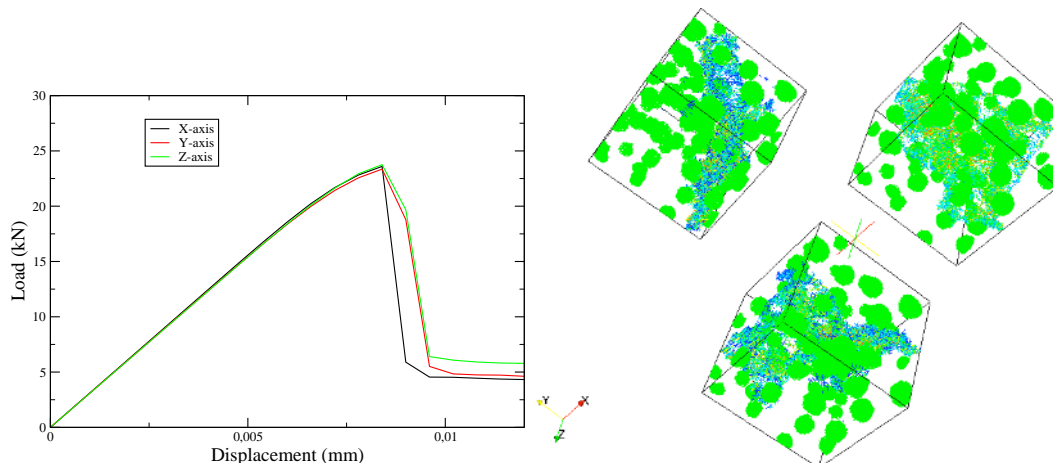

Fig. 7. 1D traction along three different axes a. macroscopic load vs displacement curve, b. micro-cracks patterns at the end of the computations

3.2.2 hydrostatic tension test

With the 1D tension test macroscopic response in hand, we turn here to the hydrostatic case. To this end we perform a tension test which consists in pulling simultaneously along X, Y and Z axis. The chosen material and geometry properties remain unchanged comparing to the 1D case (see Tab. 1). Fig. 8a plots the macroscopic load versus the imposed displacement response along the X direction obtained for the simple tension test and the hydrostatic case.

It is worth noting that the hydrostatic behavior is both more brittle and also stiffer. The macroscopic modulus along the X-direction is actually equal to a third of the macroscopic bulk modulus K and so can be related to the macroscopic Young's modulus ($E = 31000\,MPa$ computed according to the uniaxial case) and the macroscopic Poisson ratio ν,

$$3K = \frac{E}{(1 - 2\nu)} = 57\,MPa$$

leading to a $\nu = 0.228$ macroscopic Poisson ratio estimate. Fig. 8b shows micro-cracks patterns at the end of the computation. One can observe several macro-cracks contrary to a simple tensile test where only one macro-crack is observed.
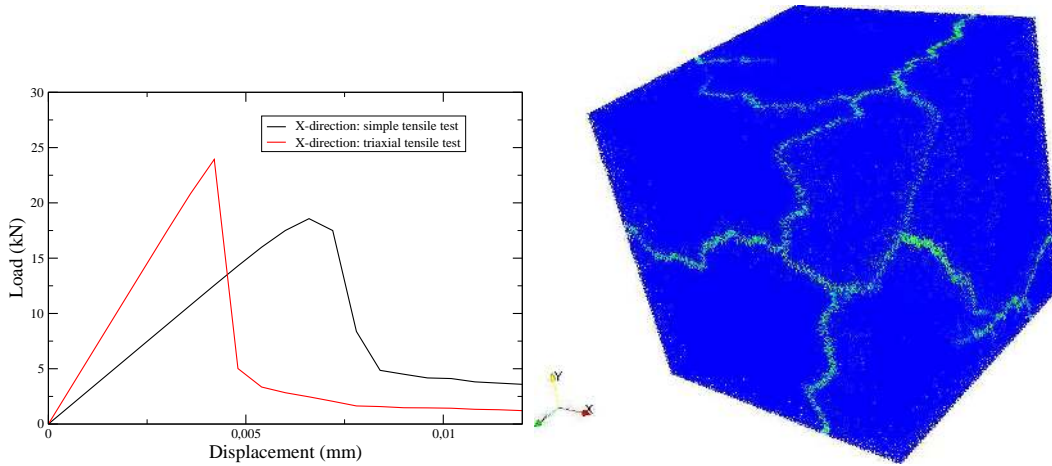

Fig. 8. Hydrostatic tension test a. macroscopic load displacement curves (1D simple tension test/hydrostatic tension test) b. micro-cracks patterns at the end of the computations

3.3 Compression test

In this part, we show the macroscopic response of the proposed model under compression loading path. Although the mesoscopic failure criterion leads to micro-cracking in tension only (see section 2.2.1 for the chosen mesoscopic failure criterion), Fig. 9a shows a macroscopic non-linear response in terms of macroscopic force versus macroscopic imposed displacement, leading to softening. Such response is mainly due to the spatial truss mesh and the macroscopic apparent Poisson effect that this geometrical representation provides. Moreover it is worth noting (see Fig. 9b) that several macro-cracks can be observed, roughly parallel to the direction of the imposed displacement. In order to compare the macroscopic responses corresponding to tension and compression, Fig. 10 plots both macroscopic load versus displacement curves. Clearly

a significant difference can be observed which is one of the major characteristics related to quasi-brittle materials like concrete. More precisely both the peak stresses (1.8 MPa in tension and 7.2 MPa in compression) as well as the amount of dissipated energies are greater in compression than in tension. Namely, the compression test leads to many more micro-cracks.
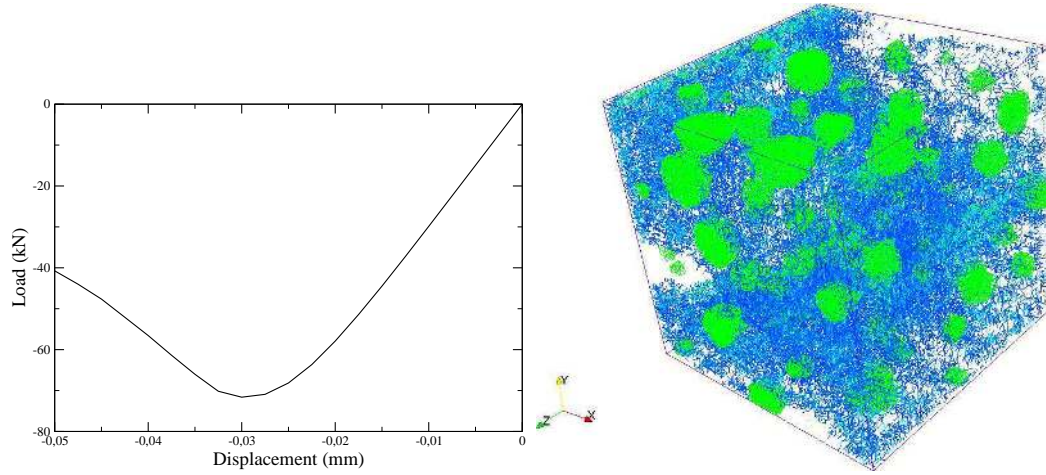

Fig. 9. Compression test a. macroscopic load vs displacement curve, b. micro-cracks patterns at the end of the computation
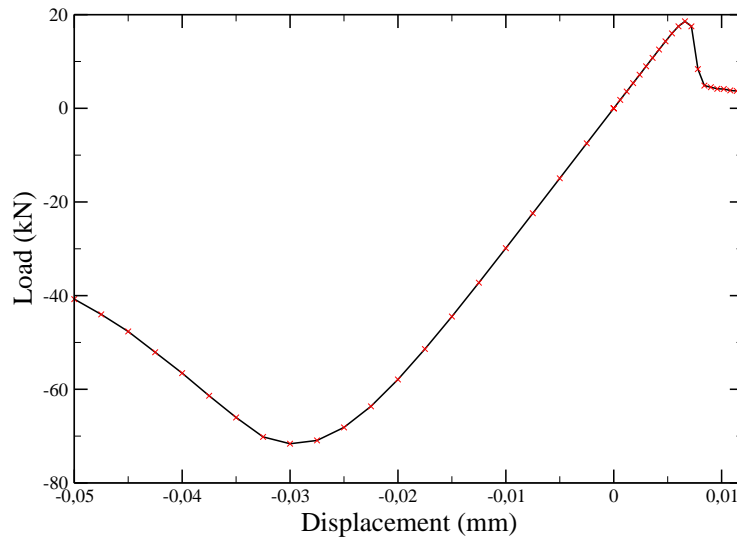

Fig. 10. Tension-Compression comparison: macroscopic load vs displacement curve

15

The last loading path we consider here deals with macroscopic shear. The set of parameters are the same as for the previous loading paths. Fig. 11 shows the micro-cracked bar elements (for whose the strong discontinuity has been activated) both from an outside point of view and an inner view as well. It is worth noting that Fig. 11 shows some kind of a single macro-crack that lies in the diagonal direction of the cube. This crack is also pictured from a different point of view: in the scaled displacement field along the X-direction where two blocks appear (sudden change of the color code) as separated by the diagonal macro-crack. Here again, although the mesoscopic failure criterion relies on tension failure mode only, the spatial truss representation as well as the explicit account for heterogeneities both lead to macroscopic failure in shear. Finally it is clear that a very small set of parameters at the mesoscopic level are enough to retrieve much more complex failure modes at the macroscale one.
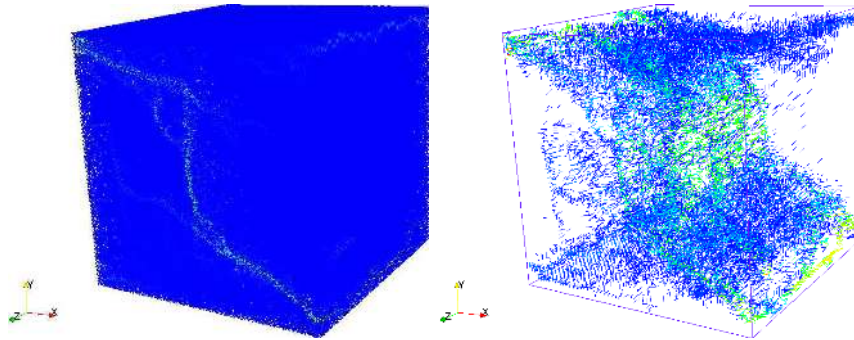

Fig. 11. Shear test: all broken elements at the end of the computation: a. surfacic view, b. inside view
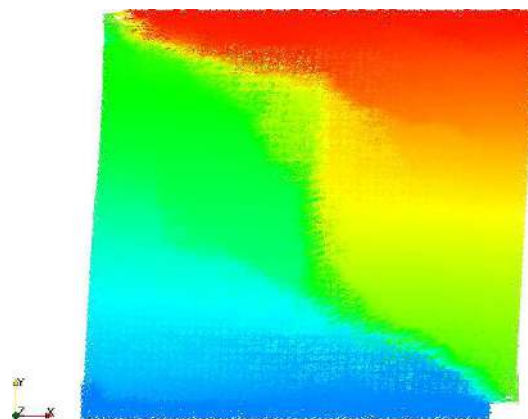

Fig. 12. Shear test: contours of displacement field in X-direction scaled by a factor 100

4   Conclusion

The usual and widespread approach when dealing with the numerical modeling of heterogeneous materials such as concrete is to implicitly work out a Representative Volume Element (RVE) thus leading to a homogeneous representation. Phenomenological models such as plasticity or damage theories are then wellknown to be both robust and easy to implement within most of FE codes and they provide a straightforward way to achieve structural analysis. However, most of the failure mechanisms that one aims to represent by using such phenomenological models are taking their very origins at a much more finer scale than the one corresponding to the RVE. For example, macro-cracks that appear before any reinforced concrete structures collapsing are preceded by a high number of micro-cracks spread in large parts of the whole structure, a few of them coalescing into macroscopic cracks. Likewise, cement-based materials macroscopic properties are known to be much influenced by their micro-cracking initial state; the latter being mainly due to strains incompatibilities between different constituants (e.g. cement paste and aggregates) during the initial drying process. Thus taking account for those heterogeneities in an explicit way (and consequently not consider an homogeneous representative volume) is a major point aiming to build predicitive and reliable numerical models.

The meso-scale model presented in this paper aims to account for heterogeneities and is adapted to model quasi-brittle materials (such as concrete) macroscopic behavior. It relies on a spatial truss mesh which is not constraint by the physical interfaces. Thus a set of bar elements might belong to two different phases and, to some extend, must be split into two parts. This issue is addressed by introducing a weak (within strain field) discontinuity inside those split elements which provides an effective and elegant way to account heterogeneities without any need for remeshing. Moreover, each element also incorporates a strong (within displacement field) discontinuity leading to the capability to represent micro-cracks opening. Such discontinuity is activated according to a dedicated failure criterion which is here chosen in order to model failure in tension only. Another key issue addressed by adding strong discontinuities is the ability to capture softening with no mesh dependency which a major issue dealing with modeling quasi-brittle materials failure. By using the Incompatible Mode Method, the implementation of both discontinuities in any FE code remain at the element level and the total number of unknowns is kept constant.

Considering different macroscopic loading paths, we finally show how the proposed model is able to provide quite complex macroscopic responses. For 1D tension the whole failure process leading to softening begins with a few diffuse micro-cracks rapidly merging to a single macro-crack splitting the specimen

into two parts. For compression, the stress field heterogeneity, due to the presence of inclusions as well as the spatial disorder mesh, leads to important diffuse micro-cracking and a large amount of dissipated energy comparing to tension. Moreover several macro-cracks can be observed thus leading to a peak macroscopic stress also more important. These two points are major features of quasi-brittle materials such as concrete.

Thus we can conclude that explicitly accounting for the heterogeneities provides great improvements for the quasi-brittle mechanical features modeling from a macroscopic point of view. Obviously many issues still need to be tackled, chief among them is to account for the probabilistic aspects directly induced by the meso-scale geometry representation. This topic is of great interest because fo being related to key issues such as RVE size computing or size-effect modeling. Moreover, in the view of getting closer from the structure point of view, great effort are currently paied in order to embed such meso-scale model within an integrated multi-scales framework.

References

[1] M. Ostoja-Starzewski. Material spatial randomness: From statistical to representative volume element. *Probabilistic Engineering Mechanics*, 21:112–132, 2006.

[2] J. Lemaitre et J.L Chaboche. Mécanique des matériaux solides. *Dunod*, 1988.

[3] J.-M. Reynouard G. Pijaudier-Cabot and J.-M. Torrenti. Mechanical behavior of concrete. *Wiley*, 2009.

[4] J.C Simo, J. Oliver, and F. Armero. An analysis of strong discontinuity induced by strain softening solutions in rate-independant solids. *Journal of Computational Mechanics*, 12:277–296, 1993.

[5] J. Oliver. Modelling strong discontinuities in solid mechanics via strain softening constitutive equations. *International Journal for Numerical Methods in Engineering*, 39:3575–3623, 1996.

[6] T. Belytschko and T. Black. Elastic growth in finite elements with minimal remeshing. *International Journal for Numerical Methods in Engineering*, 45:601–620, 1999.

[7] G.N. Wells and L.J. Sluys. Application of embedded discontinuities for softening solids. *Engineering fracture mechanics*, 65:263–281, 2000.

[8] N. Moës and T. Belytschko. Extended finite element method for cohesive crack growth. *Engineering Fracture Mechanics*, 69:813–833, 2002.

[9] G.N. Wells, L.J. Sluys, and R. de Borst. Simulating the propagation of displacement discontinuities in a regularized strain-softening medium.

International Journal for Numerical Methods in Engineering, 53:1235–1256, 2002.

[10] J. Oliver, A.E Huespe, and P.J. Sánchez. A comparative study on finite elements for capturing strong discontinuities: E-FEM vs X-FEM. *Computer Methods in Applied Mechanics and Enginnering*, 195:4732–4752, 2006.

[11] J.C Simo and M. Rifai. A class of mixed assumed strain methods and the method of incompatible modes. *International Journal for Numerical Methods in Engineering*, 29:1595–1638, 1990.

[12] A. Ibrahimbegovic and E.L Wilson. A modified method of incompatible modes. *Communications in Applied Numerical Methods*, 7:187–194, 1991.

[13] M. Klisinski, K. Runesson, and S. Sture. Finite element with inner softening band. *Journal of Engineering Mechanics*, 117:575–587, 1991.

[14] M. Hautefeuille, S. Melnyk, J.-B. Colliat, and A. Ibrahimbegovic. Failure model of heterogeneous structures using structured meshes and accounting for probability aspects. *Engineering Computations*, in press, 2009.

[15] G.N. Wells and L.J. Sluys. Analysis of slip planes in three-dimensinal solids. *Computer Methods in Applied Mechanics and Enginnering*, 190:3591–3606, 2001.

[16] J. Oliver, A.E Huespe, M.D.G Pulido, and E. Chaves. From continuum mechanics to fracture mechanics: the strong discontinuity approach. *Engineering Fracture Mechanics*, 69:113–136, 2002.

[17] D. Brancherie and A. Ibrahimbegovic. Novel anisotropic continuum-discrete damage model capable of representing localized failure of massive structures. *Computers and Structures*, 2007.

[18] K. Washizu. Variational methods in elasticity and plasticity. *Pergamon Press, New York*, 3 dition, 1982.

[19] T. Belytschko, J. Fish, and B.E. Engelmann. A finite element with embedded localization zones. *Computer Methods in Applied Mechanics and Enginnering*, 70:59–89, 1988.

[20] A. Ibrahimbegovic. Mécanique non linéaire des solides déformables: formulation théorique et résolution par éléments finis. *Lavoisier*, 2006.

[21] A. Ibrahimbegovic, F. Gharzeddine, and L. Chorfi. Classical plasticity and viscoplasticity models reformulated: theorical basis and numerical implementation. *International Journal for Numerical Methods in Engineering*, 42:1499–1535, 1998.

[22] E.L Wilson. The static condensation algorithm. *International Journal for Numerical Methods in Engineering*, 8:199–203, 1974.

[23] C. Kassiotis and M. Hautefeuille. *coFeap's Manual*, 2008. `http://www.lmt.ens-cachan.fr/cofeap/files/cofeap_manual.pdf`.

[24] R.L Taylor. *FEAP - A Finite Element Analysis Program, Programmer Manual.* University of California, Berkeley. `http://www.ce.berkeley.edu/~rlt`.

[25] R.L Taylor. *FEAP - A Finite Element Analysis Program, User Manual.* University of California, Berkeley. `http://www.ce.berkeley.edu/~rlt`.

[26] C.B. Barber, D.P. Dobkin, and H.T. Huhdanpaa. The quickhull algorithm for convex hulls. *ACM Trans. on Mathematical Software*, 22(4):469–483, 1996. `http://www.qhull.org`.